nature physics

SUPPLEMENTARY INFORMATION

https://doi.org/10.1038/s41567-020-0922-9

In the format provided by the authors and unedited.

Generalized bulk–boundary correspondence in non-Hermitian topolectrical circuits

T. Helbig[1,5], T. Hofmann[1,5], S. Imhof[2], M. Abdelghany[2], T. Kiessling[2], L. W. Molenkamp[2], C. H. Lee[3], A. Szameit[4], M. Greiter[1] and R. Thomale[1]✉

[1]Institut für Theoretische Physik und Astrophysik, Universität Würzburg, Würzburg, Germany. [2]Physikalisches Institut and Institute for Topological Insulators, Universität Würzburg, Würzburg, Germany. [3]Department of Physics, National University of Singapore, Singapore, Singapore. [4]Institut für Physik, Universität Rostock, Rostock, Germany. [5]These authors contributed equally: T. Helbig, T. Hofmann. ✉e-mail: rthomale@physik.uni-wuerzburg.de

Supplementary information to "Generalized bulk-boundary correspondence in non-Hermitian topolectrical circuits"

Tobias Helbig[1], Tobias Hofmann[1], Stefan Imhof[2], Mohamed Abdelghany[2], Tobias Kiessling[2], Laurens W. Molenkamp[2], Ching Hua Lee[3], Alexander Szameit[4], Martin Greiter[1], and Ronny Thomale[1]

[1]Institut für Theoretische Physik und Astrophysik, Universität Würzburg, D-97074 Würzburg, Germany
[2]Physikalisches Institut and Röntgen Research Center for Complex Material Systems, Universität Würzburg, D-97074 Würzburg, Germany
[3]Department of Physics, National University of Singapore, Singapore, 117542
[4]Institut für Physik, Universität Rostock, Albert-Einstein-Str. 23, 18059 Rostock, Germany

April 28, 2020

Figure captions of extended data figures

Caption Extended Data Figure 1: Frequency-dependent fit of inductances and their corresponding serial resistances $L_1, L_0, R_{L_1}, R_{L_0}$ at each experimentally studied frequencies.
Caption Extended Data Figure 2: Setup of the negative impedance converter with current inversion used in the intracell $A-B$ connection of the circuit based on an operational amplifier to generate the non-Hermitian, non-reciprocal coupling γ.
Caption Extended Data Figure 3: Spectral flow of the admittance in the complex plane at the frequency $f = 80\,\mathrm{kHz}$ for the effective model (left) and the aberration-corrected fit model (right). The flow is quantified by the parameter η, which describes the attenuation factor of the 1-20 bond.
Caption Extended Data Figure 4: Theoretically calculated and experimentally fitted magnitude of the imaginary momentum κ for the experimentally studied frequencies. Experimental values are obtained as a mean value of the exponential decay profile of all eigenmodes, that have been numerically computed from the measurement data. Their error is given by the standard deviation of the mean value while considering all eigenmodes of the system and therefore quantifies the agreement of the localization of all bulk states.
Caption Extended Data Figure 5: Top: Variation of the intracell coupling $v(\omega)$ as a function of frequency. The two OBC exceptional points for the ideal model at $v = \pm\gamma$ and the transition point at $v = 0$ with delocalized OBC modes are marked by black dashed lines. Bottom: Localization length ξ of the bulk OBC eigenmodes for the ideal effective model as a dashed red curve and for the full-scale fit model as a blue joint line. The circuit components are taken from Fig. 1 of the main text for both curves, while the parasitic resistance is chosen to $R_{L1} = 0\,\mathrm{m\Omega}$ for the red curve and to $R_{L1} = 320\,\mathrm{m\Omega}$ for the blue curve.
Caption Extended Data Figure 6: Logarithmic plot of the absolute voltage response in a measurement involving an external current feed with AC driving frequency $f = 98.5\,\mathrm{kHz}$ at the left edge of the sample at node 1 in red and at node 7 in blue. The voltage increases exponentially to the right side of the circuit due to a unit-wise amplification. The expected voltage profile normalized to the voltage at the feed node is shown as a straight line, where the slope has been numerically calculated as the average decay profile of the OBC bulk eigenmodes.

A. Non-Hermitian circuit theory

To put non-Hermitian effects in topolectric circuits on firm theoretical footing, we set up a formalism that extends the existing Hermitian formulation for grounded circuit Laplacians [1] to a more general description of linear circuit arrays.

A.1. Circuit Laplacian formulation

Grounded Circuit Laplacian. Linear circuit networks are described by a set of coupled linear ordinary differential equations with respect to time and with Dirichlet boundary conditions (see [1]). By a time-wise Fourier transform, they reduce to a set of algebraic equations. Those are represented in the frequency domain by the grounded circuit Laplacian J [1], which connects the vector of input currents $\mathbf{I}$ at the circuit nodes to the vector of node voltages $\mathbf{V}$:

$$\mathbf{I}(\omega) = J(\omega)\,\mathbf{V}(\omega). \tag{A.1}$$

The external parameter ω is set by the AC driving frequency of the system.

The Laplacian in equation (A.1) defines the complex admittance representation of the steady-state response of the circuit network to an AC current excitation with fixed frequency ω. Starting from this equilibrium, one can adopt the concept of impedance as complex resistance to perform the AC analysis of the network in the linear regime, as detailed in [1, 2] and in the following. Take a circuit of N nodes, which are labeled by the index $j = 1, \ldots, N$ while the circuit ground always retains the index 0. The nodes are assumed to feature a given connectivity, as well as an outer connection where currents I_j may enter the circuit at the j-th node. Two individual nodes of the circuit, j and l can be connected by an admittance g_{jl}, which is zero if they are not connected directly. I_{jl} with two indices shall denote the current running from node j to a directly connected node l. Kirchhoff's rule states that the current entering the circuit at node j is given by

$$I_j = \sum_{l=0}^{N} I_{jl}, \tag{A.2}$$

where $I_{jl} = g_{jl}\,(V_j - V_l)$ by using Ohm's law. Inserting this into above formula yields

$$I_j = \sum_{l=0}^{N} g_{jl}\,(V_j - V_l) = \sum_{l=1}^{N} \left(\sum_{m=1}^{N} g_{jm}\,\delta_{jl} + g_{j0}\,\delta_{jl} - g_{jl} \right) V_l \equiv \sum_{l=1}^{N} J_{jl}\,V_l. \tag{A.3}$$

The bracket defines the grounded circuit Laplacian J by its matrix representation J_{jl}. It is composed out of three parts, $J = D + W - C$. The adjacency matrix C contains the conductances between two directly connected nodes by the components

$$C_{jl} = g_{jl} \quad \text{for} \qquad j \neq l, \tag{A.4a}$$

$$C_{jj} = 0 \qquad \text{otherwise.} \tag{A.4b}$$

The total node conductance D is a diagonal matrix

$$D_{jl} = \sum_{m=1}^{N} g_{jm}\,\delta_{jl} = \sum_{m=1}^{N} C_{jm}\,\delta_{jl}, \tag{A.5}$$

where each element involves the sum of all components connected to the j-th node. The components of the ground matrix W are defined as

$$W_{jl} = g_{j0}\,\delta_{jl} \tag{A.6}$$

denoting the connections from each node to ground. The admittance values g_{jm}, that connect the nodes can consist of an arbitrary parallel or serial connection of linear components, which generally renders them complex-valued and dependent on the frequency parameter ω .

Spectral representation. We define the normalized right and left eigenvectors $\mathbf{V}_n$ and $\mathbf{U}_n^\dagger$ of the grounded circuit Laplacian J by the eigenvalue equations

$$J\,\mathbf{V}_n = j_n\,\mathbf{V}_n \tag{A.7}$$

and

$$\mathbf{U}_n^\dagger\,J = j_n\,\mathbf{U}_n^\dagger. \tag{A.8}$$

Note, that the left and right eigenvalues j_n are identical. The spectral decomposition of the circuit Laplacian into its canonical form, represented in terms of eigenvalues and eigenvectors is given by

$$J(\omega) = \sum_{n=1}^{N} j_n(\omega)\, \mathbf{V}_n(\omega)\, \mathbf{U}_n^\dagger(\omega). \tag{A.9}$$

We can equivalently decompose G into its spectral representation,

$$G(\omega) = \sum_{n=1}^{N} \frac{\mathbf{V}_n(\omega)\, \mathbf{U}_n^\dagger(\omega)}{j_n(\omega)}. \tag{A.10}$$

Admittance band structure. Consider a linear network of a d-dimensional circuit consisting of periodically repeated unit cells labeled by coordinate vectors $\mathbf{x}$ or $\mathbf{y}$ with additional sublattice degrees of freedom indicated by $\alpha, \beta \in \{1, \dots M\}$. Discrete translational invariance leads to the Laplacian's elements which depend only on the unit cell distance $J_{(\mathbf{x},\alpha),(\mathbf{y},\beta)} = J_{\alpha,\beta}(\mathbf{x}-\mathbf{y})$. The unit cell structure can be diagonalized by the spatial Fourier transformation to reciprocal space,

$$\mathcal{FT} : J(\mathbf{k}) = \sum_{\mathbf{x}} e^{-i\mathbf{k}\mathbf{x}}\, J(\mathbf{x}), \tag{A.11}$$

resulting in the matrix equation

$$\mathbf{I}(\omega, \mathbf{k}) = J(\omega, \mathbf{k})\, \mathbf{V}(\omega, \mathbf{k}) \tag{A.12}$$

with remaining sublattice degrees of freedom. By diagonalizing the $(M \times M)$-matrix $J(\omega, \mathbf{k})$, we find the eigenstates $\mathbf{V}_m(\omega, \mathbf{k})$ and the admittance eigenvalues $j_m(\omega, \mathbf{k})$, which constitute the complex-valued admittance band structure of M bands at each wave vector $\mathbf{k}$ and parametrically depend on the external frequency ω.

Greens function. To find the response of a circuit system to an external excitation in the shape of an input current at one or several nodes, we invert equation (A.1) through the Greens function $G(\omega) = J^{-1}(\omega)$. It relates the current and voltage vectors via

$$\mathbf{V}(\omega) = G(\omega)\, \mathbf{I}(\omega) \tag{A.13a}$$

or, in terms of an additional momentum parameter $\mathbf{k}$ in reciprocal space,

$$\mathbf{V}(\omega, \mathbf{k}) = G(\omega, \mathbf{k})\, \mathbf{I}(\omega, \mathbf{k}), \tag{A.13b}$$

where $G(\omega, \mathbf{k})$ be the spatial Fourier transform of the Greens function [2]. The poles of the Greens function $G(\omega, \mathbf{k})$ are the eigenfrequencies of the circuit system. Those determine the dynamical behavior of the circuit system, where each voltage eigenmode is associated with a resonance frequency, at which it oscillates in time. Alternatively, the resonances can be found as the frequency roots of the Laplacian eigenvectors $j_n(\omega) \stackrel{!}{=} 0$ using the frequency dependence of the admittances. Note, that the dependence on the parameter ω will be left implicitly in the following.

A.2. Circuit symmetries

Hermiticity. In an electrical circuit, a resistor that is represented by the real part of the Laplacian introduces dissipation to the system. Being the inverse of conductance, an electrical resistance measures the opposition to the *flow* of an electrical current. This thermodynamic process of converting electrical energy into Joule heat is non-reversible. In contrast, the electrical reactance describes the opposition to the *change* of an electrical current or voltage, in the form of a capacitive or inductive component. A passive, imaginary contribution to the circuit Laplacian conserves the total energy in the system. This motivates the definition of a Hermitian circuit system by the anti-Hermiticity of its defining Laplacian matrix,

$$J^\dagger = -J, \qquad J^\dagger(\mathbf{k}) = -J(\mathbf{k}) \tag{A.14}$$

in real and reciprocal space. A Hermitian circuit is thus one that possesses a fully imaginary admittance band structure, $j_n \in (i\,\mathbb{R})$. Its eigenfrequency spectrum is fully real, $\omega_n \in \mathbb{R}$ since it is a Hermitian system. Circuit Hermiticity can typically be broken by the inclusion of passive resistive or active non-reciprocal reactive elements. In a Hermitian system, left and right eigenvectors are identical, $\mathbf{V}_n = \mathbf{U}_n$.

Reciprocity. We define circuit reciprocity in a synthetic lattice structure as a symmetry operation, which "inverts" the couplings, *i.e.* interchanges connections in between nodes to go in the opposite direction. With this definition, circuit reciprocity can only be broken if some connections are not bidirectionally symmetric. As a visualization, consider two nodes of the circuit with labels j and l connected by a passive element. The current flowing out of node j must equal the current entering at node l. In other words, the current running from j to l, I_{jl}, is the negative of the current running from l to j, *i.e.* $I_{jl} = -I_{lj}$. This symmetry is called circuit reciprocity. Henceforth, breaking reciprocity necessitates a current feed or sink to be implemented across a connection between two nodes of the circuit.

Mathematically, circuit reciprocity is equivalent to invariance under transposition:

$$J^\top = J, \qquad J^\top(\mathbf{k}) = J(-\mathbf{k}). \tag{A.15}$$

It then follows that the spectrum of J obeys

$$j_n(\mathbf{k}) = j_n(-\mathbf{k}), \tag{A.16}$$

i.e. is reflection symmetric in reciprocal space with every eigenvalue being at least two-fold degenerate. A reciprocal system relates left and right eigenvectors by a complex conjugation,

$$\mathbf{V}_n = \mathbf{U}_n^*. \tag{A.17}$$

In a Hermitian system, they are additionally real and therefore equal. The Greens function G of a reciprocal system is also symmetric, $G^\top = G$. The eigenfrequencies in a reciprocal system obey the general relation $\omega(\mathbf{k}) = \omega(-\mathbf{k})$, which means that the dispersion of left and right traveling waves is identical.

As discussed in Section C.2, the combined breaking of reciprocity and Hermiticity is a necessary condition for the non-Hermitian skin effect, which is the central theme of our experiment.

Time-reversal symmetry. As an abstract transformation, time reversal acts by inverting the direction of time, $t \to -t$. Resistances, which are represented by the real part in the Laplacian lead to time reversal symmetry breaking in any arrangement. They experience a potential drop converting electrical energy into heat, which is an irreversible process. Consequently, a circuit is time-reversal symmetric, if only if it does not possess any resistive parts. This condition can be conceived in terms of the circuit Laplacian in real and reciprocal space by

$$J^* = -J, \qquad J^*(\mathbf{k}) = -J(-\mathbf{k}), \tag{A.18}$$

leading to the constraint

$$j_n(\mathbf{k}) = -j_n^*(-\mathbf{k}) \tag{A.19}$$

for the $\mathbf{k}$-dependent spectrum of J. Translated into real space, we find an eigenvalue $-j_n^*$ for every eigenvalue j_n of the Laplacian, if j_n is not fully imaginary. This implies that the Laplacian eigenvalues are symmetric with respect to the real axis. Its eigenvectors satisfy

$$\mathbf{V}(-\mathbf{k}) = -\mathbf{V}^*(\mathbf{k}), \tag{A.20}$$

i.e. the operation of time reversal (complex conjugation and sign inversion) relates the eigenvectors of $J(\mathbf{k})$ at opposite momenta $\mathbf{k}$ and $-\mathbf{k}$. The resonances of a time-reversal symmetric system appear as complex conjugated pairs. Applied to $\mathbf{k}$-space, we obtain a solution $\omega^*(-\mathbf{k})$ for every solution $\omega(\mathbf{k})$.

B. Derivation of the effective circuit model

Derivation of the circuit Laplacian. We design a topolectric circuit, that breaks both Hermiticity and reciprocity to study the breakdown of bulk-boundary correspondence and the emergence of the non-Hermitian Skin effect. Its unit cell is schematically depicted in Fig. 1c along with the corresponding circuit board cutout in Fig. 1d of the main text. Based on the definitions in Appendix A.1, we derive the Laplacian matrix of every single circuit component, that enters the unit cell in Fig. 1c of the main text, which taken together form the full Laplacian of the system. As mentioned in Appendix A.1, we work in the linear regime, where the complex admittances as the inverse of impedances of capacitors, resistors and inductors are given by $i\omega C$, $1/R$ and $1/(i\omega L)$, respectively.

The circuit contains intracell connections between node A and B of capacitance C_1 and inductance L_1. Considering only this connection, an input current at node A or B in the unit cell with position x relates to the voltages at the nodes by

$$\left.\begin{aligned} I_{\mathrm{A}}(x) &= \left(i\omega C_1 + \frac{1}{i\omega L_1}\right)\left(V_{\mathrm{A}}(x) - V_{\mathrm{B}}(x)\right) \\ I_{\mathrm{B}}(x) &= \left(i\omega C_1 + \frac{1}{i\omega L_1}\right)\left(V_{\mathrm{B}}(x) - V_{\mathrm{A}}(x)\right) \end{aligned}\right\} \Rightarrow \begin{pmatrix} I_{\mathrm{A}}(x) \\ I_{\mathrm{B}}(x) \end{pmatrix} = \sum_{x'} \left(i\omega C_1 + \frac{1}{i\omega L_1}\right) \begin{pmatrix} \delta_{x,x'} & -\delta_{x,x'} \\ -\delta_{x,x'} & \delta_{x,x'} \end{pmatrix} \begin{pmatrix} V_{\mathrm{A}}(x') \\ V_{\mathrm{B}}(x') \end{pmatrix},$$

where the current-voltage relation is written as a matrix equation on the right-hand side. This defines the reduced Laplacian for the elements C_1 and L_1, which is Hermitian, time-reversal symmetric and reciprocal.

Analogously, the capacitance C_2 connects adjacent unit cells and therefore involves voltages of different sublattice type and neighboring unit cell index. An input current I_{A} or I_{B} splits up into the voltage difference

$$\left.\begin{aligned} I_{\mathrm{A}}(x) &= i\omega C_2\left(V_{\mathrm{A}}(x) - V_{\mathrm{B}}(x-1)\right) \\ I_{\mathrm{B}}(x) &= i\omega C_2\left(V_{\mathrm{B}}(x) - V_{\mathrm{A}}(x+1)\right) \end{aligned}\right\} \Rightarrow \begin{pmatrix} I_{\mathrm{A}}(x) \\ I_{\mathrm{B}}(x) \end{pmatrix} = \sum_{x'} i\omega C_2 \begin{pmatrix} \delta_{x,x'} & -\delta_{x-1,x'} \\ -\delta_{x+1,x'} & \delta_{x,x'} \end{pmatrix} \begin{pmatrix} V_{\mathrm{A}}(x') \\ V_{\mathrm{B}}(x') \end{pmatrix},$$

where the sum is again used to define the reduced Laplacian for C_2, which now contains off-diagonal elements in real space of unit cells. It is further Hermitian, time-reversal symmetric and reciprocal.

The breaking of Hermiticity and reciprocity is achieved by a single coupling in a particular way with an INIC element of capacitance C_3. We engineer this connection such that it acts as a negative capacitance of $-C_3$ as viewed from sublattice node A and as a regular positive capacitance C_3 as viewed from sublattice B. This necessitates the use of active circuit components in order to break the bidirectional symmetry of passive components, which is circuit reciprocity. The required current source or sink for this element can be realized by the use of an operational amplifier in a negative feedback configuration, which is detailed in Appendix D.2. As an intracell coupling, its current-voltage relations are given by

$$\left.\begin{aligned} I_{\mathrm{A}}(x) &= -i\omega C_3\left(V_{\mathrm{A}}(x) - V_{\mathrm{B}}(x)\right) \\ I_{\mathrm{B}}(x) &= \quad i\omega C_3\left(V_{\mathrm{B}}(x) - V_{\mathrm{A}}(x)\right) \end{aligned}\right\} \Rightarrow \begin{pmatrix} I_{\mathrm{A}}(x) \\ I_{\mathrm{B}}(x) \end{pmatrix} = \sum_{x'} i\omega C_3 \begin{pmatrix} -\delta_{x,x'} & \delta_{x,x'} \\ -\delta_{x,x'} & \delta_{x,x'} \end{pmatrix} \begin{pmatrix} V_{\mathrm{A}}(x') \\ V_{\mathrm{B}}(x') \end{pmatrix},$$

where the reduced Laplacian of the INIC component C_3 violates reciprocity and Hermiticity, but preserves time-reversal symmetry.

Lastly, node A is grounded by a capacitance C_0 and both nodes A and B by an inductance L_0 and a resistance R_0. With the ground node being at zero potential, the currents from node A and B to ground read

$$\left.\begin{aligned} I_{\mathrm{A}}(x) &= \left(i\omega C_0 + \frac{1}{i\omega L_0} + \frac{1}{R_0}\right)\left(V_{\mathrm{A}}(x) - 0\right) \\ I_{\mathrm{B}}(x) &= \left(\frac{1}{i\omega L_0} + \frac{1}{R_0}\right)\left(V_{\mathrm{B}}(x) - 0\right) \end{aligned}\right\} \Rightarrow \begin{pmatrix} I_{\mathrm{A}}(x) \\ I_{\mathrm{B}}(x) \end{pmatrix} = \sum_{x'} \left(\frac{1}{i\omega L_0} + \frac{1}{R_0}\right) \begin{pmatrix} \delta_{x,x'} & 0 \\ 0 & \delta_{x,x'} \end{pmatrix} \begin{pmatrix} V_{\mathrm{A}}(x') \\ V_{\mathrm{B}}(x') \end{pmatrix}$$
$$+ \sum_{x'} \left(i\omega C_0\right) \begin{pmatrix} \delta_{x,x'} & 0 \\ 0 & 0 \end{pmatrix} \begin{pmatrix} V_{\mathrm{A}}(x') \\ V_{\mathrm{B}}(x') \end{pmatrix},$$

where the effective Laplacian for the grounding elements is fully diagonal and preserves reciprocity, Hermiticity and time-reversal symmetry.

Transformation to reciprocal space. To arrive at the final circuit Laplacian for the model, we assume a periodic arrangement of unit cells, which converts to a translation symmetry of the underlying Laplacian, $J(x, x') = J(x - x')$. The periodic Laplacian, whose couplings only depend on the difference between unit cell positions

$\bar{x}$ can be Fourier transformed with (A.11), which diagonalizes the Laplacian up to the sublattice degrees of freedom. The only off-diagonal real space connection is given by C_2, which transforms as

$$J_2(x) = i\omega C_2 \begin{pmatrix} \delta_{x,0} & -\delta_{x,1} \\ -\delta_{x,-1} & \delta_{x,0} \end{pmatrix} \quad \xrightarrow{\mathcal{FT}} \quad J_2(k) = i\omega C_2 \begin{pmatrix} 1 & -e^{-ik} \\ -e^{ik} & 1 \end{pmatrix}$$

for every wave vector label k. Putting the Fourier transformation of all the individual connections together results in the Laplacian

$$\begin{aligned} J(k) = i\omega \Bigg[& \left(C_1 - \frac{1}{\omega^2 L_1} \right) \begin{pmatrix} 1 & -1 \\ -1 & 1 \end{pmatrix} + C_2 \begin{pmatrix} 1 & -e^{-ik} \\ -e^{ik} & 1 \end{pmatrix} + C_3 \begin{pmatrix} -1 & 1 \\ -1 & 1 \end{pmatrix} - \frac{i}{\omega R_{\mathrm{x}}} \begin{pmatrix} 1 & -1 \\ -1 & 1 \end{pmatrix} \\ & - \left(\frac{1}{\omega^2 L_0} + \frac{i}{\omega R_0} \right) \begin{pmatrix} 1 & 0 \\ 0 & 1 \end{pmatrix} + C_0 \begin{pmatrix} 1 & 0 \\ 0 & 0 \end{pmatrix} \Bigg], \end{aligned} \tag{B.1}$$

which can be further simplified in its form to be written as an effective model, that contains the relevant physics.

Mapping to effective circuit model. We choose $C_0 = 2C_3$, factor out a term $i\omega$ and simplify the frequency-dependent form of the Laplacian by rewriting it in terms of the unit matrix and the three Pauli matrices σ_x, σ_y, σ_z to

$$\begin{aligned} J(k) = i\omega \Bigg[& \left(C_1 + C_2 + C_3 - \frac{1}{\omega^2} \left(\frac{1}{L_0} + \frac{1}{L_1} \right) - \frac{i}{\omega R_0} \right) \mathbb{1} \\ & - \left(C_1 - \frac{1}{\omega^2 L_1} + C_2 \cos(k) \right) \sigma_x - (C_2 \sin(k) - i\, C_3)\, \sigma_y \Bigg] \end{aligned} \tag{B.2a}$$

$$\begin{aligned} = i\omega \Bigg[& \left(C_1 \left(1 - \frac{\omega_0^2}{\omega^2} \right) + C_2 + C_3 - \frac{1}{\omega^2\, L_0} - \frac{i}{\omega R_0} \right) \mathbb{1} \\ & - \left(C_1 \left(1 - \frac{\omega_0^2}{\omega^2} \right) + C_2 \cos(k) \right) \sigma_x - (C_2 \sin(k) - i\, C_3)\, \sigma_y \Bigg]. \end{aligned} \tag{B.2b}$$

The parallel intracell connection of the inductance L_1 and the capacitance C_1 forms an LC resonating circuit with its resonance frequency $\omega_0 = 1/\sqrt{L_1 C_1}$. This allows us to rewrite the inductive part L_1 in terms of the capacitive part C_1 in the second line of the above equation. At the resonance $\omega = \omega_0$, the $L_1 C_1$ resonator exhibits an impedance divergence and blocks any current of flowing through the element.

We observe that the INIC connection enters the Laplacian as a non-reciprocal term proportional to $i\sigma_y$, which breaks Hermiticity due to a complex prefactor of the Pauli matrix. In our design, we choose the inductance L_0 to ground in such a way, that the imaginary part of the prefactor to the unit matrix vanishes at the resonance ω_0 of the $L_1 C_1$ resonator. This can be achieved by taking

$$L_0 = \frac{1}{\omega_0^2\,(C_2 + C_3)} = L_1 \cdot \frac{C_1}{C_2 + C_3}. \tag{B.3}$$

We thus arrive at the final Laplacian of the circuit model,

$$\begin{aligned} J(k) = i\omega \Bigg[& \left((C_1 + C_2 + C_3) \left(1 - \frac{\omega_0^2}{\omega^2} \right) - \frac{i}{\omega R_0} \right) \mathbb{1} \\ & - \left(C_1 \left(1 - \frac{\omega_0^2}{\omega^2} \right) + C_2 \cos(k) \right) \sigma_x - \left(C_2 \sin(k) - i\, C_3 \right) \sigma_y \Bigg] \\ & = i\omega\, \epsilon_0(\omega)\, \mathbb{1} - i\omega \Big[\big(\underbrace{v(\omega) + r\cos(k)}_{\equiv h_x} \big) \sigma_x + \big(\underbrace{r \sin(k)}_{\equiv h_y} - i\gamma \big)\, \sigma_y \Big] \\ & = i\omega\, \epsilon_0(\omega)\, \mathbb{1} - \omega\, \bar{J}(k), \end{aligned} \tag{B.4}$$

where $\bar{J}(k)$ is the effective Laplacian that contains the essential physics, which we intend to investigate. It depends on the parameters

$$\epsilon_0(\omega) = (C_1 + C_2 + C_3) \left(1 - \frac{\omega_0^2}{\omega^2} \right) - \frac{i}{\omega R_0}, \quad v = v(\omega) = C_1 \left(1 - \frac{\omega_0^2}{\omega^2} \right), \quad r = C_2, \quad \gamma = C_3. \tag{B.5}$$

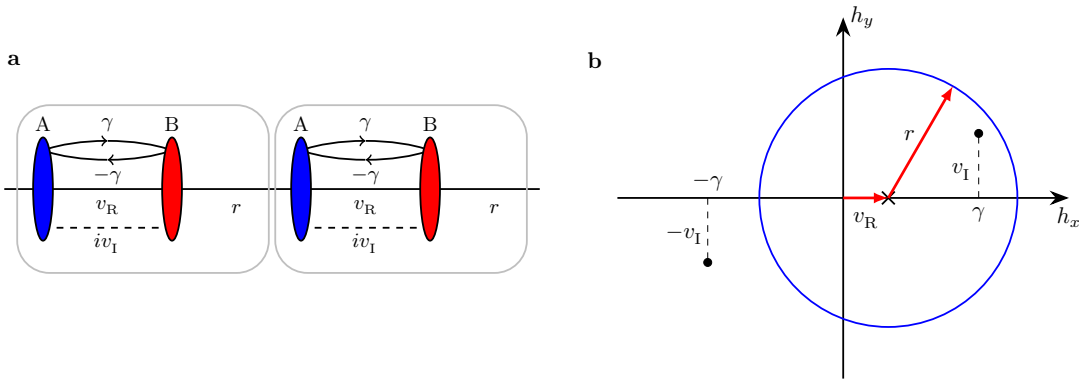

Figure S1: **(a)** Reduced hopping model described by the effective Laplacian of the circuit model. The magnitude of the intracell connection v is modulated by the AC driving frequency ω, the non-reciprocity necessary for the skin effect is implemented by γ. **(b)** Exceptional points in the effective circuit model in the (h_x, h_y)-plane at the parameter choices and k-points, where $(h_x, h_y) = \pm(\gamma, v_I)$.

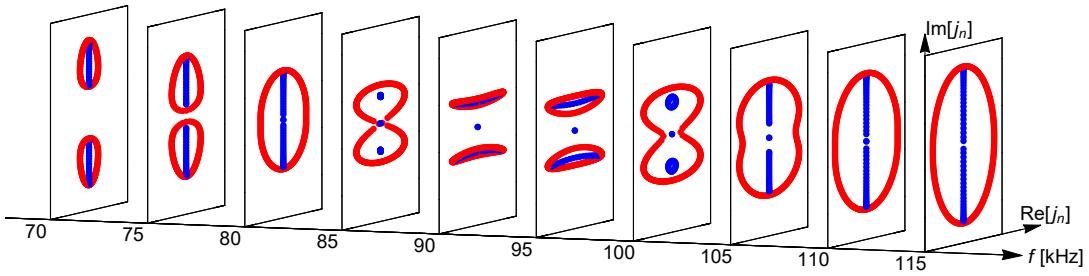

Figure S2: Admittance spectrum of the ideal effective hopping model $\bar{J}(k)$ without parasitic corrections in the complex plane as a function of frequency in steps of 5 kHz with PBCs as red and OBCs as blue dots. The PBC spectrum forms closed loops, that merge to open arcs for OBCs. In the frequency sweep, we encounter two frequencies with exceptional points at $f \approx 80\,\mathrm{kHz}$ and $f \approx 100\,\mathrm{kHz}$, as well as a transition frequency at $f \approx 90\,\mathrm{kHz}$, where bulk-boundary correspondence is restored. The circuit components are chosen to $C_1 = 300\,\mathrm{nF}$, $L_1 = 10.1\,\mu\mathrm{H}$, $C_2 = 94\,\mathrm{nF}$, $C_3 = 47\,\mathrm{nF}$, $L_0 = 33\,\mu\mathrm{H}$.

The Laplacian in equation (B.4) is equivalent to equation (1) of the main text and corresponds to the experimental setting of our circuit.

To finalize the effective description, we omit the contribution $\epsilon_0(\omega)$ as it is proportional to the unit matrix and accounts to a shift of the eigenvalues by a frequency-dependent constant while leaving the eigenvectors invariant. In our model, $\epsilon_0(\omega)$ has no effect on the physics of the non-Hermitian skin effect. However, the precise diagonal grounding terms are still crucial to the experimental implementation, as they control the global stability of the circuit system (see Sec. D.3). We have also rescaled the effective Laplacian by factoring out a term ω, which is a global prefactor that induces a frequency-dependent scale on the eigenvalues. The complex eigenvalues of the effective Laplacian $\bar{J}$ for periodic as well as open boundary conditions are plotted in Fig. S2 as a function of the frequency parameter $f = \omega/(2\pi)$. The OBC spectrum looks fundamentally different to the PBC spectrum, realizing a non-perturbative spectral flow from closed loops to open arcs. Associated with that is the localization of all bulk modes at one boundary of the system, called the non-Hermitian Skin effect and discussed in SI C.2.

Inclusion of parasitic effects. To map the theoretical calculations with experimental data, we extend the effective description to a full-scale fit model that takes into account the parasitic resistances in the inductive couplings as the most prominent experimental imperfections. For this, we adjust the inductances according to $L_j \to L_j + R_{L_j}/(i\omega)$, with $j = \{0, 1\}$, where R_{L_j} denotes the serial resistance of the inductor L_j. This amounts

to a complex extension of the intracell coupling $v(\omega)$ in the effective model, which is modified to

$$v(\omega) \to \left(C_1 - \frac{L_1}{\omega^2\, L_1^2 + R_{L_1}^2} \right) + \; i \; \left(-\frac{1}{\omega^2} \cdot \frac{R_{L_1}}{\omega^2\, L_1^2 + \; R_{L_1}^2} \right) \equiv v_{\mathrm{R}} + i\, v_{\mathrm{I}}, \tag{B.6}$$

while the other parameters remain unchanged. Regarding the full Laplacian in equation (B.4), the unit matrix coefficient which describes a global complex shift of the admittance eigenvalues transforms as

$$\begin{aligned} \epsilon_0(\omega) &= \left(C_1 + C_2 + C_3 - \frac{1}{\omega^2 L_0} - \frac{1}{\omega^2 L_1} - \frac{i}{\omega R_0} \right) \\ &\to \left(C_1 + C_2 + C_3 - \frac{1}{\omega^2 L_0 - i\omega R_{L_0}} - \frac{1}{\omega^2 L_1 - i\omega R_{L_1}} - \frac{i}{\omega R_0} \right) \end{aligned} \tag{B.7}$$

due to the incorporation of parasitic resistances. The black dots in Fig. S3 show admittance eigenvalue measurements at different external driving frequencies ω and for periodic boundary conditions of the experimental circuit setup, which are also depicted as points in the complex plane in Fig. 2b of the main text. In the experimental implementation, parasitic resistances and tolerances in the circuit components enter, which lead to small deviations as compared to the band structure given by $J(k)$ in equation (B.4). For reference, the parasitics corrected theoretical admittance bands are shown as grey curves in Fig. S3.

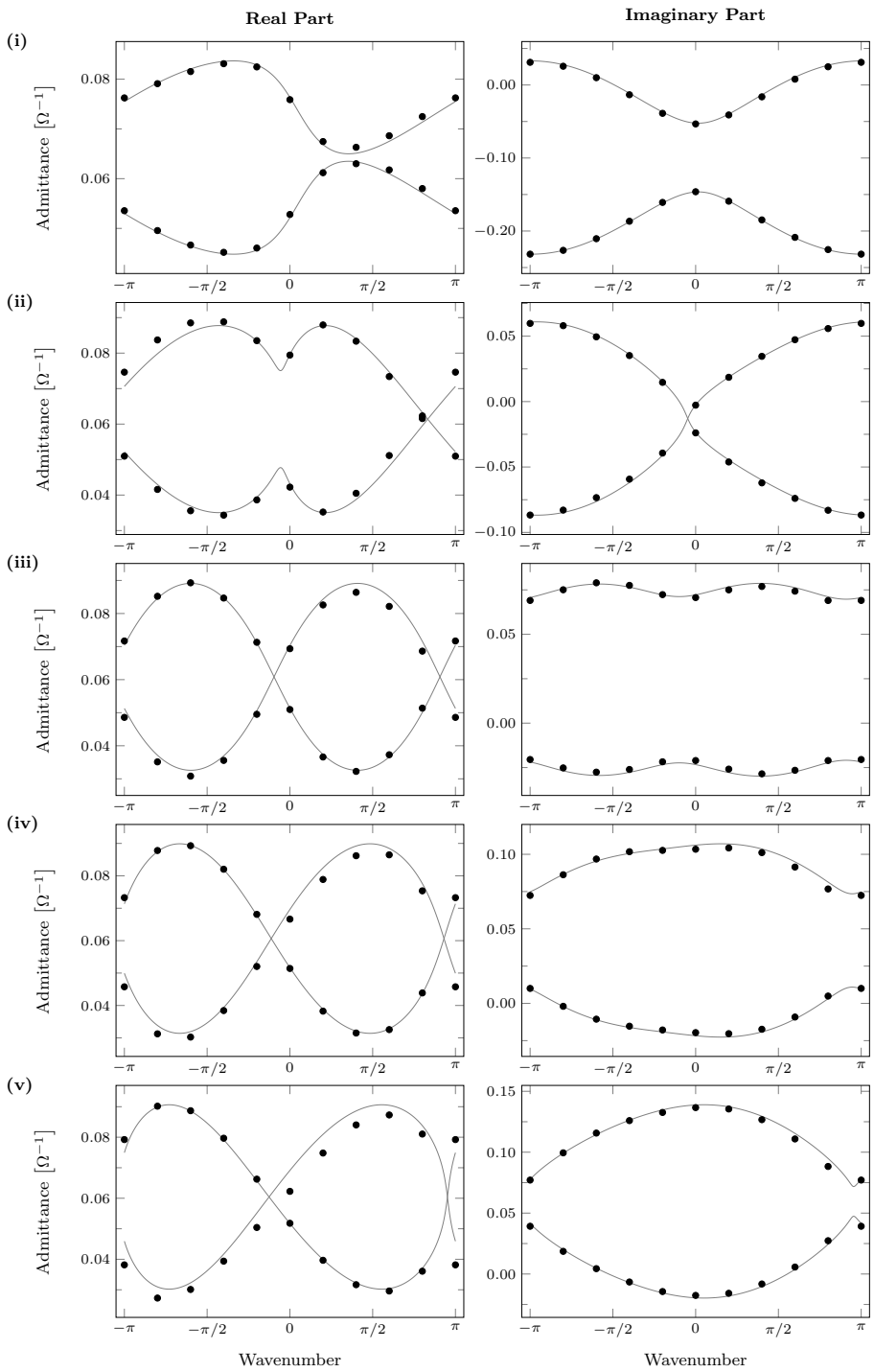

Figure S3: Real and imaginary part of the wave vector resolved admittance band structure for AC frequencies $f_{(\mathrm{i})} = 70.0\,\mathrm{kHz}$, $f_{(\mathrm{ii})} = 84.2\,\mathrm{kHz}$, $f_{(\mathrm{iii})} = 91.5\,\mathrm{kHz}$, $f_{(\mathrm{iv})} = 95.0\,\mathrm{kHz}$, and $f_{(\mathrm{v})} = 98.5\,\mathrm{kHz}$ of the circuit model given in the main text and in equation (B.4). Discrete dots denote experimental data, joint lines show the parasitics-corrected theoretical band predictions.

C. Properties of the model

The (parasitics-corrected) effective circuit model $\bar{J}(k)$ is equivalent a one-dimensional tight-binding model, whose hopping connectivity is schematically represented in Fig. S1a. A similar model with $\sigma_y \leftrightarrow \sigma_z$ has been theoretically studied in [3]. The Hermitian part of $\bar{J}$ is form-invariant to a one-dimensional SSH model with two sublattices, an intracell hopping of v_R, and a hopping of r in between unit cells. Our non-Hermitian and non-reciprocal effective model extends the SSH model by two terms. First, we introduce a non-Hermitian term $iv_\mathrm{I}\,\sigma_x$ due to parasitic adjustments, that is symmetric, *i.e.* reciprocal, and appears as an imaginary hopping element between sublattice A and B inside the unit cell. Second, we add a term $-i\gamma\,\sigma_y$, which breaks the combination of circuit reciprocity and Hermiticity and gives rise to the non-Hermitian skin effect. We study the properties of this model in detail in the following.

C.1. Exceptional points

Properties of exceptional points. A non-Hermitian circuit can exhibit complex admittance eigenvalues instead of fully imaginary ones in a Hermitian circuit. The non-Hermiticity gives rise to complex eigenvalue degeneracies, which are band touchings of at least two complex-valued bands. Consider the spectrum of the effective Laplacian $\bar{J}(k)$ given by

$$\bar{j}_\pm(k) = \pm\, i\,\sqrt{\left(v_\mathrm{R} + r\cos(k) + iv_\mathrm{I}\right)^2 + \left(r\sin(k) - i\gamma\right)^2}. \tag{C.1}$$

It features exceptional points if either γ or v_R is nonzero. Exceptional points occur at eigenvalue degeneracies, whose geometric multiplicity is smaller than their algebraic multiplicity, rendering the system non-diagonalizable. This is equivalent to the fact, that the eigenvectors corresponding to the degenerate exceptional point eigenvalue do not span the full subspace.

In general, exceptional points occur in a square- or higher root behavior as a function of some parameter of the system. This leads to a branch cut of the spectrum in parameter space and to a non-trivial winding of eigenmodes. If the root behavior is a function of the wave vector $\mathbf{k}$, it allows us to access the corresponding branch cut in the complex-valued band structure. Assuming a (2×2)-matrix, a degenerate eigenvalue automatically implies non-diagonalizability, as the transformed diagonal matrix would be proportional to the unit matrix, which is related only to itself in a similarity transformation. This holds in extension to higher dimensional matrices, whose size is equivalent to the multiplicity of an eigenvalue degeneracy.

Conditions for exceptional points under PBC. We define $(d_x, d_y) \coloneqq (h_x + iv_\mathrm{I}, h_y - i\gamma)$, such that $\bar{J}(k) = i\,\mathbf{d}\cdot\boldsymbol{\sigma}$. An exceptional point in the spectrum occurs, if the conditions

$$\mathfrak{Re}\left(\mathbf{d}\right)\cdot\mathfrak{Im}\left(\mathbf{d}\right) = 0 \quad \wedge \quad \left|\mathfrak{Re}\left(\mathbf{d}\right)\right| = \left|\mathfrak{Im}\left(\mathbf{d}\right)\right| \tag{C.2}$$

are simultaneously fulfilled. In the effective model, those conditions combine to

$$v_\mathrm{I}\,\left(v_\mathrm{R} + r\cos(k)\right) = r\gamma\sin(k) \tag{C.3a}$$

$$v_\mathrm{R}^2 + r^2 + 2v_\mathrm{R} r\cos(k) = v_\mathrm{I}^2 + \gamma^2, \tag{C.3b}$$

which in terms of (h_x, h_y) are given by

$$h_x = v_\mathrm{R} + r\cos(k) \stackrel{!}{=} \pm\gamma \tag{C.4a}$$

$$h_y = r\sin(k) \stackrel{!}{=} \pm v_\mathrm{I}. \tag{C.4b}$$

The two constraints are visualized in Fig. S1b, As we place ourselves in the two-dimensional parameter space $\mathbf{h} = (h_x, h_y)^\top$, the components of h_x and h_y parametrize a circle for $k \in [0{,}2\pi]$ with the origin located at $(h_x, h_y) = (v_\mathrm{R}{,}0)$ and a radius given by r. Exceptional points mark the band closing of a complex-valued band structure of the non-Hermitian model, as given in Fig. S2 at $f \approx 85\,\mathrm{kHz}$. They occur, when the circle in the $\mathbf{h}$-plane intersects one of the points $\pm(\gamma, v_\mathrm{I})^\top$, that are highlighted in Fig. S1b. The resulting (2×2)-Laplacian at the corresponding intersecting k-point reduces to a defective matrix with a two-fold degenerate exceptional point at zero. The two eigenstates in that degenerate subspace coalesce to one. They do not form a complete basis and the non-Hermitian Laplacian is no longer diagonalizable. Both PBC exceptional points in the $\mathbf{h}$-space can only be simultaneously reached, if $v_\mathrm{R} = 0$ and r is adjusted accordingly.

Exceptional points under OBC. The OBC spectrum exhibits an exceptional point, if $|v_\mathrm{R}| = |\gamma|$ and $v_\mathrm{I} = 0$ simultaneously. This occurs at the two frequencies $f \approx 85\,\mathrm{kHz}$ and $f \approx 100\,\mathrm{kHz}$ in Fig. S2. There, the PBC spectrum forms two distinct loops with a touching point at zero admittance, if $r = 2\gamma$. The OBC spectrum is contracted to three points, which are all exceptional. At $|v_\mathrm{I}| = |v_\mathrm{R}|$, the asymmetry between left and right moving modes, that is introduced by the γ-term attains full-scale leading to maximally localized eigenmodes for OBC. In Fig. S1b, it corresponds to the center of the PBC circle residing at the exceptional point ($\pm\gamma$,0) in $\mathbf{h}$-space. The special parameter choice of $r = 2\gamma$ includes the other exceptional point in the PBC spectrum, which turns out to be advantageous for the experimental circuit implementation. We can analytically compute the OBC eigenvalues of a system with N unit cells at the exceptional point (here: $v_\mathrm{R} = -\gamma$ and $v_\mathrm{I} = 0$) by considering the determinant

$$\det\big(\lambda\mathbb{1} - \bar{J}_\mathrm{OBC}\big) = \underbrace{\begin{vmatrix} \lambda & 2i\gamma & 0 & & & & \\ 0 & \lambda & -ir & 0 & & & \\ 0 & -ir & \lambda & 2i\gamma & 0 & & \\ & 0 & 0 & \lambda & -ir & 0 & \\ & & 0 & -ir & \lambda & 2i\gamma & 0 \\ & & & & \ddots & \ddots & \ddots \end{vmatrix}}_{:= A_N \,\in\, \mathbb{C}^{(2N)\times(2N)}} = \lambda \cdot \underbrace{\begin{vmatrix} \lambda & -ir & 0 & & & \\ -ir & \lambda & 2i\gamma & 0 & & \\ 0 & 0 & \lambda & -ir & 0 & \\ & 0 & -ir & \lambda & 2i\gamma & 0 \\ & & & \ddots & \ddots & \ddots \end{vmatrix}}_{:= B_N \,\in\, \mathbb{C}^{(2N-1)\times(2N-1)}}. \tag{C.5}$$

With the two definitions of the matrices A_N and B_N and the identity $\det(A_N) = \lambda \cdot \det(B_N)$, it follows, that

$$\begin{aligned} \det\big(\lambda\mathbb{1} - \bar{J}_\mathrm{OBC}\big) &= \lambda \cdot \Big[\lambda \underbrace{\det(A_{N-1})}_{=\lambda\cdot\det(B_{N-1})} - (ir)^2 \cdot \det(B_{N-1})\Big] = \lambda\,\left(\lambda^2 - (ir)^2\right)\det(B_{N-1}) \\ &= \lambda\,\left(\lambda^2 - (ir)^2\right)^{N-1} \underbrace{\det(B_1)}_{=\lambda} = \lambda^2\,\left(\lambda^2 - (ir)^2\right)^{N-1}. \end{aligned} \tag{C.6}$$

For $v_\mathrm{R} = \gamma$ or $v_\mathrm{R} = -\gamma$, the OBC spectrum consists out of three points, $\lambda_1 = 0$, which is two-fold degenerate and $\lambda_2 = +ir$, $\lambda_3 = -ir$ which each are $(N-1)$-fold degenerate, adding up to the total algebraic multiplicity of $2N$.

All three eigenvalues possess a geometric multiplicity of one, where the eigenvectors are given by

$$\mathbf{x}_1 = \big(1, \quad 0, \quad 0, \quad 0, \quad 0, \quad \cdots\big)^\top, \tag{C.7a}$$

$$\mathbf{x}_2 = \big(1, \quad -\tfrac{r}{2\gamma}, \quad -\tfrac{r}{2\gamma}, \quad 0, \quad 0, \quad \cdots\big)^\top, \tag{C.7b}$$

$$\mathbf{x}_3 = \big(1, \quad \tfrac{r}{2\gamma}, \quad -\tfrac{r}{2\gamma}, \quad 0, \quad 0, \quad \cdots\big)^\top. \tag{C.7c}$$

for $v_\mathrm{R} = -\gamma$. At the exceptional points for $v_\mathrm{R} = +\gamma$, the eigenmodes retain the same profile, but are localized on the opposing edge. Those eigenvectors obtain the largest possible localization as $\xi_0 \to 0$ for $|v_\mathrm{R}| \to |\gamma|$. A perturbative parameter adjustment close to the exceptional point leads to small modifications of the eigenstates, which lifts the geometric degeneracy and upgrades the eigenbasis to its full dimension, where all eigenvectors are localized on the same edge. We refer to this as the non-Hermitian skin effect, which remains valid for $v_\mathrm{R} \neq 0$.

C.2. The non-Hermitian skin effect

Breakdown of bulk-boundary correspondence. If $\gamma, v_\mathrm{R} \neq 0$ in

$$\bar{J}(k) = i\Big(\big(v_\mathrm{R} + iv_\mathrm{I} + r\cos(k)\big)\sigma_x + \big(r\sin(k) - i\gamma\big)\,\sigma_y\Big), \tag{C.8}$$

we observe a breakdown of the bulk-boundary correspondence (BBC), which is manifested as a localization of all bulk modes at the boundary of the system under OBCs, known as the non-Hermitian skin effect [4]. In Hermitian systems, the influence of a single coupling is treated as a $1/N$ perturbative effect in an N-site system. In non-Hermitian systems featuring the skin effect, the same local coupling modification leads to a substantial change of *extensively* many states. A necessary condition for this is the conspired breaking of reciprocity and Hermiticity.

Imaginary flux argument. To understand the effect, we thread an imaginary magnetic flux through the sample. A magnetic flux ϕ through the periodic ring of lattice sites couples to the system through a translation of the momentum vector $k \to k + \phi/N$. In a tight-binding system, it can be attached to the lattice couplings by a spatially constant phase factor $e^{i\phi/N}$. It can be gauge transformed to affect only the N-1 boundary coupling by the phase $e^{i\phi}$, as long as the total phase acquired by the particle moving along the ring in a closed path remains unchanged. An analytic continuation to $\phi \in \mathbb{C}$ and consequently $k \in \mathbb{C}$ defines an interpolation between periodic and open boundary conditions (PBCs and OBCs) with $\mathfrak{Im}\,[\phi]$ increasing from 0 to ∞. This complex flux threading transforms the spectrum according to

$$j(k) \to j(k+\phi) = j\left(k + \frac{1}{N}\,\mathfrak{Re}\,[\phi] + i\,\frac{1}{N}\,\mathfrak{Im}\,[\phi]\right). \tag{C.9}$$

In a finite system, the momentum is discretized to $k \in [0, \frac{2\pi}{N}, \ldots, 2\pi\,(1 - \frac{1}{N})]$. Appropriate choices of $\mathfrak{Re}\,[\phi]$ can (a) interpolate to intermediate values of k and (b) permute the eigenvalues in an adiabatic flux pumping from 0 to 2π. Note, that in such a case only the association of eigenstates to eigenvalues can be permuted, while the total PBC spectrum must stay invariant. $\mathfrak{Im}\,[\phi]$ not only modulates the strength of the $N-1$ connection, but also physically corresponds to a spatially decaying wave function.

Spectral flow from PBC to OBC. A non-Hermitian system generally features complex eigenvalues, which we plot as points in the complex plane or as a complex contour for continuous k. Under PBCs, they must trace out a closed curve due to the periodicity in k, *i.e.* $j(k+2\pi) = j(k)$. If the system additionally preserves reciprocity, the eigenvalues delineate an arc as they retrace themselves due to the condition $j(k) = j(-k)$. If the system is non-reciprocal, but Hermitian, the eigenvalues are still confined to an interval along the real axis. Only the combined breaking of Hermiticity and reciprocity allows the PBC spectrum to lie on one or more closed loops with nonzero interior areas.

As $\mathfrak{Im}\,[\phi]$ increases towards the OBC limit ($\mathfrak{Im}\,[\phi] \to \infty$), the closed loops shrink to zero since the effect of threading $\mathfrak{Re}\,[\phi] \to \mathfrak{Re}\,[\phi] + 2\pi$ is weakened in the boundary couplings, $e^{i\phi} = e^{-\mathfrak{Im}\,[\phi]} e^{i\mathfrak{Re}\,[\phi]}$. Hence, in the full OBC limit, the eigenvalues must eventually converge along points or arcs which cannot be shrunk further, and cannot lie on closed loops or curves anymore [5, 6].

In general, the limiting OBC spectral arc or point is reached at a finite $\mathfrak{Im}\,[\phi] \equiv \kappa$. Using the point or arc degeneracy, it can be determined as the smallest value of $\mathfrak{Im}\,[\phi]$ such that the complex band gap closes, with

$$j(k + i\kappa) = j(k' + i\kappa) \tag{C.10}$$

for $k \neq k'$ with $k, k' \in \mathbb{R}$. As κ affects all momentum eigenstates, all PBC bulk modes become skin modes for OBC that are localized near either the left or right boundary with localization length κ^{-1}. Non-Hermitian systems, whose PBC eigenvalues already trace out open arcs in the complex plane cannot exhibit the skin effect for OBC.

In our circuit implementation, recirocity is broken by the term $i\gamma\sigma_y$, which amplifies the transmission in one direction and weakens that in the other. Under PBCs, the system supports delocalized Bloch states, which all localize as skin states on either edge under OBCs.

We calculate the localization length of the skin modes in the parasitics-corrected model. Consider the eigenvalue equation for $\bar{J}$ with open boundary conditions,

$$\bar{J}_{\mathrm{OBC}}\,\psi = \lambda\,\psi, \tag{C.11}$$

where $\psi = (\psi_{1,\mathrm{A}}, \psi_{1,\mathrm{B}}, \psi_{2,\mathrm{A}} \ldots)^\top$. In the bulk of the system, the eigenvalue equation is given by

$$ir\,\psi_{x-1,\mathrm{B}} + i(v_\mathrm{R} + iv_\mathrm{I} - \gamma)\,\psi_{x,\mathrm{B}} = \lambda\,\psi_{x,\mathrm{A}} \tag{C.12a}$$

$$i(v_\mathrm{R} + iv_\mathrm{I} + \gamma)\,\psi_{x,A} + ir\,\psi_{x+1,A} = \lambda\,\psi_{x,B}. \tag{C.12b}$$

By assuming a Bloch ansatz $(\psi_{x,\mathrm{A}}, \psi_{x,\mathrm{B}}) = \alpha^x(u_\mathrm{A}, u_\mathrm{B})$, $\alpha \in \mathbb{C}$ the bulk equations reduce to

$$i\big(\alpha^{-1}\,r + (v_\mathrm{R} + iv_\mathrm{I} - \gamma)\big)u_\mathrm{B} = \lambda\,u_\mathrm{A}, \tag{C.13a}$$

$$i\big((v_\mathrm{R} + iv_\mathrm{I} + \gamma) + r\,\alpha\big)u_\mathrm{A} = \lambda\,u_\mathrm{B}, \tag{C.13b}$$

which combine to form

$$\begin{aligned}\lambda^2 &= -\left[(v_\mathrm{R} + iv_\mathrm{I} - \gamma) + \alpha^{-1}\right]\cdot\left[(v_\mathrm{R} + iv_\mathrm{I} + \gamma) + r\,\alpha\right] \\ &= -\left[v_\mathrm{R}^2 + 2iv_\mathrm{R}v_\mathrm{I} - v_\mathrm{I}^2 - \gamma^2 + r^2 + r\,v_\mathrm{R}\,(\alpha + \alpha^{-1}) + ir\,v_\mathrm{I}\,(\alpha + \alpha^{-1}) - r\,\gamma\,(\alpha - \alpha^{-1})\right].\end{aligned} \tag{C.14}$$

As expected, we recover the PBC spectrum of the effective Laplacian by replacing α with the Bloch factor $\alpha \to e^{ik}$.

Upon multiplication by α, equation (C.14) defines a quadratic equation in α, yielding two distinct solutions, α_1 and α_2. A rearrangement of equation (C.14) using the solutions yields

$$\alpha_1 \cdot \alpha_2 = \frac{v_\mathrm{R} + iv_\mathrm{I} + \gamma}{v_\mathrm{R} + iv_\mathrm{I} - \gamma}. \tag{C.15}$$

As detailed in [6], the OBC modes exist at the largest value of $|\alpha|$, where the magnitude of the two solutions agrees, resulting in

$$|\alpha_1| = |\alpha_2| = |\alpha| = \sqrt{\left|\frac{v_\mathrm{R} + iv_\mathrm{I} + \gamma}{v_\mathrm{R} + iv_\mathrm{I} - \gamma}\right|} = \sqrt[4]{\frac{(v_\mathrm{R} + \gamma)^2 + v_\mathrm{I}^2}{(v_\mathrm{R} - \gamma)^2 + v_\mathrm{I}^2}} \tag{C.16}$$

for the magnitude of the Bloch factor. At this value of $|\alpha|$, the OBC spectrum is reached. We can map this result to the localization length of the localized bulk modes for OBC by a complex extension of the wave vector $k \to k + i\kappa$, which is described in equation (C.10). By increasing κ, we deform the PBC spectrum away from a closed loop up to the point, where $|\alpha_1| = |\alpha_2|$ and the eigenvalues meet on an open arc. At this point, all bulk modes obtain the Bloch factor $|\alpha|$ and are consequently localized on the boundary of the system and labeled as skin modes. κ then determines the localization length of the skin modes as they decay from the edge with $e^{-n/\xi}$,

$$\xi = \left(\frac{1}{4}\ln\frac{(v_\mathrm{R} - \gamma)^2 + v_\mathrm{I}^2}{(v_\mathrm{R} + \gamma)^2 + v_\mathrm{I}^2}\right)^{-1}, \tag{C.17}$$

where n labels the unit cells of the system, as counted in positive (here: left to right) x-direction. The localization length ξ does not depend on the intercell coupling r, but the concrete form of the eigenvectors is modified by r. If $v_\mathrm{I} = 0$, the localization length reads

$$\xi_0 = \left(\frac{1}{2}\ln\left|\frac{v_\mathrm{R} - \gamma}{v_\mathrm{R} + \gamma}\right|\right)^{-1}, \tag{C.18}$$

and the skin modes obtain the maximal localization for $|v_\mathrm{R}| = |\gamma|$, where $\xi_0 \to 0$. The signs of v_R and γ determine the localization of the modes,

$$\begin{aligned} &\xi > 0, \quad \text{if } \mathrm{sgn}\left(\frac{v_\mathrm{R}}{\gamma}\right) < 0 \quad \Rightarrow \quad \text{left edge localization,} \\ &\xi < 0, \quad \text{if } \mathrm{sgn}\left(\frac{v_\mathrm{R}}{\gamma}\right) > 0 \quad \Rightarrow \quad \text{right edge localization.} \end{aligned}$$

Restoration of bulk-boundary correspondence. There is a special transition point at $v_\mathrm{R} = 0$, where the localization of the skin modes switches from one side to the other. At this special point, all modes are localized due to a divergence in the localization length $\xi \to \infty$. The vanishing of the skin effect at this fine-tuned point roots in the fact, that the PBC spectrum in the complex plane already forms an open arc. The BBC is restored, because the PBC and the OBC spectrum lies on the same arc, resulting in a trivial spectral flow with $\kappa = 0$. The admittance spectrum at this point is depicted in Fig. S2 for $f \approx 90\,\mathrm{k}$. It occurs despite the simultaneous breaking of reciprocity and Hermiticity. Intuitively, it is based on the sole phase difference of the non-reciprocal intracell hopping, connected through $e^{i\pi}$ in a reversion of its direction. The magnitude of $\bar{J}$ is reciprocal and does not establish any preference in direction. In mathematical terms, the PBC lying on an open arc can be understood through the *extended reciprocity condition,*

$$\exists\ k_\mathrm{s} \in [0,2\pi] \text{ with } E(k_\mathrm{s} + k) = E(k_\mathrm{s} - k), \tag{C.19}$$

stating that the PBC spectrum is reciprocal with respect to a wave vector k_s. If such a k_s exists, the spectrum must trace out an arc and BBC is restored and hence there is no skin effect. A necessary, but not sufficient condition for the skin effect is that there must not exist such a k_s. In the effective circuit model $\bar{J}$, the PBC spectrum is symmetric around $k_s = \pi/2$ for $v_\mathrm{I} = 0$ and $v_\mathrm{R} = 0$, leading to valid BBC and delocalized bulk modes for both PBC and OBC.

C.3. Topological modes

Topological regime. To study the topological character of the circuit, we map the OBC Laplacian to an effective reciprocal lattice model, that respects the BBC. For this, we use the parameter

$$\alpha = \sqrt{\frac{v_\mathrm{R} + i v_\mathrm{I} + \gamma}{v_\mathrm{R} + i v_\mathrm{I} - \gamma}}, \tag{C.20}$$

which can be viewed as a modification of the boundary hopping element as well as a complex extension of the wave vector k. We similarity transform [4] the effective OBC Laplacian to

$$\bar{J}'_\mathrm{OBC} = S^{-1} \bar{J}_\mathrm{OBC} S, \tag{C.21}$$

where $S = \mathrm{diag}(1, \alpha, \alpha, \alpha^2, \ldots, \alpha^N)$ in a system with N unit cells. Note, that this transformation is identical to an analytical continuation of the wave vector $k \to k + i \ln(|\alpha|)$. We arrive at a one-dimensional chain that is form-invariant to the SSH hopping model, given by

$$\bar{J}' = i \left[(t_0 + r \cos(k))\, \sigma_x + (r \sin(k))\, \sigma_y \right] \tag{C.22}$$

for PBCs. The intracell hopping is transformed to $t_0 = \sqrt{(v_\mathrm{R} + i v_\mathrm{I})^2 - \gamma^2}$ and is now reciprocal, while the intercell hopping r remains invariant. However, the SSH model in (C.22) can pick up complex coefficients, where

$$t_0 \in \ \mathbb{R}, \ \text{if } |v_\mathrm{R}| > |\gamma| \ \wedge \ v_\mathrm{I} = 0, \tag{C.23a}$$
$$t_0 \in i\,\mathbb{R}, \ \text{if } |v_\mathrm{R}| < |\gamma| \ \wedge \ (v_\mathrm{I} = 0 \ \vee \ v_\mathrm{R} = 0)\,, \tag{C.23b}$$
$$t_0 \in \ \mathbb{C}, \ \text{if } \ v_\mathrm{I} \neq 0 \ \wedge \ v_\mathrm{R} \neq 0. \tag{C.23c}$$

The spectrum of the SSH model is given by

$$\bar{j}'_\pm = \pm i \sqrt{t_0^2 + r^2 + 2\, t_0\, r\, \cos(k)}, \tag{C.24}$$

which is fully imaginary if t_0 is real and complex valued if t_0 is imaginary or complex valued. As we terminate the chain with whole unit cells, we get two zero energy solutions if the intracell hopping is smaller than the intercell hopping, $|t_0| < |r|$, and none if $|t_0| > |r|$. The zero energy solutions are related to topological midgap modes, which are exponentially localized at the boundary, and take the form

$$\psi_0^\mathrm{L} \sim \left(1, \quad 0, \quad -\tfrac{t_0}{r}, \quad 0, \quad (\tfrac{t_0}{r})^2, \quad \ldots\right), \tag{C.25a}$$
$$\psi_0^\mathrm{R} \sim \left(\ldots, \quad (\tfrac{t_0}{r})^2, \quad 0, \quad -\tfrac{t_0}{r}, \quad 0, \quad 1\right), \tag{C.25b}$$

upon neglecting finite-size contributions. The states are localized with a localization length of $\xi_0 = (\ln|r/t_0|)^{-1}$ on both edges. The topological phase transition of the model is found at $|t_0| = |r|$, where the band gap of the fully imaginary spectrum closes and the zero energy eigenvalue disappears. It is given by $\bar{j}'_\pm = 0$ and simplifies to

$$t_0^2 = r^2 \quad \Leftrightarrow \quad v_\mathrm{R} = \pm\sqrt{r^2 + \gamma^2} \tag{C.26}$$

for $v_\mathrm{I} = 0$. This condition is consistent with Fig. S2 with $v_\mathrm{I} = 0$ for frequencies between $f \approx 80\,\mathrm{kHz}$ and $f \approx 110\,\mathrm{kHz}$, where we observe a topological zero admittance mode in the blue OBC spectrum. Going back to the original model $\bar{J}$, we know, that the eigenvalue equation

$$\bar{J}'_\mathrm{OBC}\, \psi'_\mathrm{OBC} = \bar{j}'_\mathrm{OBC}\, \psi'_\mathrm{OBC} \tag{C.27}$$

transforms to

$$\bar{J}_\mathrm{OBC} \left(S\psi'_\mathrm{OBC} \right) = \bar{j}'_\mathrm{OBC} \left(S\psi'_\mathrm{OBC} \right). \tag{C.28}$$

The functions $S\psi'_\mathrm{OBC}$ are eigenfunctions of the original effective model to the eigenvalues $\bar{j}'_\mathrm{OBC}$, which stay invariant under the transformation. We can directly relate the topological transition property to the effective model, which hosts two zero energy eigenvalues and corresponding modes for $|v_\mathrm{R}| < \sqrt{\sqrt{r^4 - (2\gamma v_\mathrm{I})^2} - v_\mathrm{I}^2 + \gamma^2}$.

The identification of the topological regime and the associated phase transition expected from a bulk analysis (band closing of the PBC spectrum at exceptional points) are parametrically distorted due to the non-Hermiticity. The eigenmodes retain zero energy upon neglecting finite-size contributions. Except for the topological modes, all eigenstates of $\bar{J}'$ are delocalized for both OBC and PBC, because BBC is restored and there are no skin modes. All bulk modes of $\bar{J}$ are then localized at one edge due to the transformation property of eigenmodes, $S\psi'_{\mathrm{OBC}}$. Their localization length can be directly read off as

$$\xi = (\ln|\alpha|)^{-1}\,, \tag{C.29}$$

because at every second entry in $S\psi'_{\mathrm{OBC}}$, the exponential of $|\alpha|$ increases by one power, leading to a decay of the states from the edge into the bulk. As far as the topological modes are concerned, it is not valid to use the approximate form of ψ_0^{L} and ψ_0^{R} and transform it with S, because the boundary coupling plays an essential role in $\bar{J}$ and the finite-size contribution can not be neglected anymore. Due to the strong asymmetry originating from the γ-term, both topological states are localized at one edge of the system and coalesce to one state at the OBC exceptional point, $|\gamma| = |v_{\mathrm{R}}|$.

D. Details on experimental implementation

D.1. Observables in topolectrical circuits

In an experimental circuit setup, the node voltages and input currents are direct observables. The input currents $\mathbf{I}$ are immediately controlled by the voltage or current sources used to excite the circuit, the node voltages $\mathbf{V}$ can be interpreted as the response of the circuit system to this excitation. The Laplacian matrix J connects these observables, $\mathbf{I} = J\mathbf{V}$. Its inverse, the Greens function $G = J^{-1}$, can be understood as the circuit's response function. In principle, both, time-resolved or steady-state measurements of voltages and currents are feasible, however, in linear circuit models frequency-resolved steady-state measurements using lock-in techniques are sufficient to analyse the behaviour of the circuit. Since the amplitude of the excitation does not influence the response function in linear circuits, complex impedances or admittances are meaningful observables, *i.e.* ratios of currents and voltages. In the following paragraphs the relations between observables and admittance eigenvalues/eigenstates are computed. The aim is to identify observables which are suitable to detect the anomalous extensive localization of the eigenstates. As we will show, simple impedance measurements are not sufficient to detect the skin effect, instead a non-local voltage response can be used. Finally, a full reconstructing of all eigenvalues and eigenstates is always a possibility in circuit networks.

Notation. In the following the right (left) eigenstates of the Laplacian matrix are denoted by $\mathbf{V}_n$ ($\mathbf{U}_n$) with $n = 1, \cdots, N$ in a system with N circuit nodes. The corresponding n-th eigenvalue is labelled by j_n, the Greens function by G, and the dependence on the frequency ω of all quantities is implicitly assumed.

Two-point impedance. One of the simplest observables are measurements of the impedance between two circuit nodes a and b. This is possible by creating a voltage difference between the nodes and measuring the current running through the voltage source. If the voltages measured at nodes a and b are denoted by V_a and V_b, respectively, the two-point impedance is given by

$$Z_{ab} = \frac{V_a - V_b}{I}, \tag{D.1}$$

where I is the current leaving the circuit at node a and re-entering at node b. The two-point impedance can be written in terms of the eigenvectors reading

$$Z_{ab} = \sum_{n=1}^{N} \frac{(V_{n,a} - V_{n,b}) \cdot (U_{n,a} - U_{n,b})^*}{j_n}. \tag{D.2}$$

Note, that it depends on both left and right eigenmodes and is a *reciprocal* quantity, $Z_{ab} = Z_{ba}$. Therefore, it is not possible to use the two-point impedance to detect localization of eigenmodes for the skin effect model: If the right eigenvectors are localized on the right edge of the circuit, the corresponding left eigenvectors are localized at the left edge. Since left and right eigenvectors compensate each other according to equation (D.2), the two-point impedance does neither retrieve information about the localization of the right eigenvectors nor of the left eigenvectors.

The same arguments apply to a single-point impedance Z_{a0} measured between one node a and ground. It is given in terms of the eigenvectors by

$$Z_{a0} = \sum_n \frac{1}{j_n} \mathrm{V}_{n,a}\, \mathrm{U}^*_{n,a}. \tag{D.3}$$

Following the above reasons, the single-point impedance measurement is not useful to detect the eigenmode localization for the skin effect model presented in this work.

Non-local voltage response. The voltage response $\mathbf{V}$ of a circuit to a current excitation $\mathbf{I}$ can hint to the localization properties of the eigenmodes. Using the Greens function G the voltage response can be computed as

$$\mathbf{V} = G\,\mathbf{I} = \sum_n \frac{1}{j_n} \mathbf{V}_n \left(\mathbf{U}_n^\dagger\, \mathbf{I}\right) = \sum_n \frac{1}{j_n} \mathbf{V}_n \left(\sum_a U^*_{n,a} I_a\right). \tag{D.4}$$

This means that the resulting response $\mathbf{V}$ is a superposition of all right eigenvectors $\mathbf{V}_n$ each weighted with the inverse of its admittance eigenvalue and the effective excitation, the scalar product of the corresponding left eigenvector $\mathbf{U}_n$ with the vector of excitation currents $\mathbf{I}$.

For a periodic system with extended eigenstates, one would expect a delocalized voltage response to a local current excitation (only one input current) according to equation (D.4). As the following calculation shows, this is not true if parasitic resistances are present. Due to them the complex spectrum gets shifted to larger real parts. To a first approximation the admittance eigenvalues can be written as

$$j_n \sim \frac{1}{\rho} + \epsilon_n, \tag{D.5}$$

where ρ is a value of the dimension of a resistance which quantifies the mean shift of the spectrum due to resistive effects. ϵ_n represents the original spectrum without the shift. If $1/\rho \gg |\epsilon_n|$, the Greens function can be expanded in $\rho\epsilon_n$ for large parasitic resistances yielding

$$G = \rho \sum_n \mathbf{V}_n \mathbf{U}_n^\dagger - \sum_n (\rho^2 \epsilon_n) \mathbf{V}_n \mathbf{U}_n^\dagger + \mathcal{O}\left(\rho^3 \epsilon_n^2\right) = \rho\, \mathbb{1} - \sum_n (\rho^2 \epsilon_n) \mathbf{V}_n \mathbf{U}_n^\dagger + \mathcal{O}\left(\rho^3 \epsilon_n^2\right). \tag{D.6}$$

Since the left and right eigenvectors form a complete basis (except at exceptional points), the Greens function is to 0-th order proportional to the identity. This means that the voltage response for large resistances is proportional to the current excitation, $\mathbf{V} \sim \rho \mathbf{I} + \cdots$. Thus, naturally any voltage response to a single-point current excitation would be local in a periodic circuit. If all voltage eigenmodes are delocalized, e.g. as it would be the case in a periodic network, all orders of G except for the 0-th contribute in a delocalized response profile. The contribution from $\mathbf{V} \sim \rho \mathbf{I}$ results in a local voltage response to a single-point excitation $\mathbf{I}$ even for an arbitrarily small damping $1/\rho$.

By implication, we can use this observation to test if the eigenmodes of our circuit implementation are indeed localized at one boundary. We excite the circuit at the edge where the eigenmodes are not expected to localize and measure the voltage response. If the damping is sufficiently small, the voltage response is localized at the opposing edge. In a circuit consisting of periodically repeated unit cells this is only possible if the right eigenvectors are localized at the edge. Therefore, measuring a non-local voltage response is the smoking gun for the existence of skin modes. The data to this experiment is presented in Fig. 3 of the main text.

Spectral reconstruction. The most natural observation technique to identify the localization properties of eigenmodes is to reconstruct them. In the Laplacian formalism of periodic circuit arrays it is possible to reconstruct the admittance eigenvalues and eigenmodes from voltage and current measurements. This was first explored in [2]. The spectral reconstruction for PBC and OBC involve a series of measurements steps. The PBC results are acquired by feeding an input current to sublattice A and measuring the voltage at all nodes, then repeating the same procedure for sublattice B. The spectrum is then calculated through Fourier transformation, which is possible due to circuit periodicity [2]. For the OBC spectra, the current is fed at each node individually and the voltages of all nodes were measured. The results of these measurements are used to populate the Greens function, as the inverse of the Laplacian,

$$\mathbf{V} = \begin{pmatrix} G_{1,m}\, I_m \\ \vdots \\ G_{N,m}\, I_m \end{pmatrix} = \begin{pmatrix} G_{1,1} & \cdots & G_{1,N} \\ \vdots & \ddots & \vdots \\ G_{N,1} & \cdots & G_{N,N} \end{pmatrix} \cdot \begin{pmatrix} 0 \\ \vdots \\ I_m \\ \vdots \\ 0 \end{pmatrix} \qquad \Leftrightarrow \qquad G_{n,m} = \frac{V_n}{I_m}, \tag{D.7}$$

where I_m is the excitation current at node m, and V_n is the measured voltage at node n. Using this construction, the eigenvalues and eigenvectors can be computed numerically, in analogy to [2]. In total, under PBC two current and $2N$ voltage measurements are necessary. For OBC N current and N^2 voltage measurements are required.

D.2. Implementation of the INIC

For the realization of the negative impedance converter through current inversion (INIC) we employ an operational amplifier (opamp) in the configuration shown in Fig S4. An opamp is a differential amplifier, *i.e.* its output voltage V_0 is proportional to the difference of the positive $V_{\text{in},+}$ and negative input potential $V_{\text{in},-}$, $V_0 = A\,(V_{\text{in},+} - V_{\text{in},-})$, with the amplification A being much larger than unity. The opamp is operated in negative feedback configuration, which means that its output is coupled to its inverting (negative) input via an impedance Z_-. In negative feedback configuration the opamp stabilizes the voltages such that $V_{\text{in},+} = V_{\text{in},-}$. If the input voltage difference deviates from zero, e.g. the positive input potential is larger than the potential at the negative input, the output voltage increases. This leads to an increased voltage at the inverting input via the

negative feedback loop such that the input voltage difference decreases. As a rule of thumb for this mechanism to work the negative feedback admittance $1/Z_-$ must be larger than the positive feedback admittance $1/Z_+$ (for further operability and stability considerations see Sec. D.3, D.3, and D.4).

After some initial oscillations, we can assume $V_{\mathrm{in},+} = V_{\mathrm{in},-}$. This means for the INIC circuit that the potential at the inverting input equals the input voltage V_1, which is set by the voltage of the node the INIC is connected to (see Fig. S4). To derive the Laplacian matrix for the INIC element, we calculate the input currents I_1 and I_2 in dependence of the node voltages V_1 and V_2 and the output voltage V_0 of the opamp, assuming virtual V_1 at the inverting input. This yields

$$I_1 = \frac{1}{Z_+}\left(V_1 - V_0\right), \tag{D.8a}$$

$$I_2 = i\omega C\left(V_2 - V_1\right), \tag{D.8b}$$

where we defined the total impedance in the positive feedback loop as Z_+ and the total impedance of the negative feedback loop as Z_-. Since the currents flowing into the inputs of the opamp are very small, approximately zero, we find as well

$$I_2 = \frac{1}{Z_-}\left(V_1 - V_0\right). \tag{D.9}$$

Using these relations one can eliminate the opamp's output potential V_0 from the equations and obtain

$$I_1 = -i\omega C\,\frac{Z_-}{Z_+}\left(V_1 - V_2\right), \tag{D.10a}$$

$$I_2 = i\omega C\left(V_2 - V_1\right). \tag{D.10b}$$

The currents do not fulfil the reciprocity condition $I_1 = -I_2$ as for a passive circuit element. The current flowing into the INIC at the left is different from the current coming out at the right. The opamp acts as a source or drain for currents, which is possible as it is an active circuit element.

We can re-write the relations between the currents and the node voltages in the matrix formalism defining the Laplacian of the INIC as

$$\begin{pmatrix} I_1 \\ I_2 \end{pmatrix} = i\omega C \begin{pmatrix} -\nu & \nu \\ -1 & 1 \end{pmatrix} \begin{pmatrix} V_1 \\ V_2 \end{pmatrix} \tag{D.11}$$

with $\nu = Z_-/Z_+$ being the ratio of negative and positive feedback loop impedance. For our experimental implementation of the INIC we choose the positive and negative feedback loop impedances to be equal and given by a resistor R_a in parallel to a capacitor C_a (see Fig. 1 of the methods section). This realization was chosen after advanced stability considerations elaborated in Sec. D.4. Our choice implies $\nu = 1$, such that I_1 equals I_2 instead of $-I_2$ for a passive circuit element. Hence, reciprocity is broken. In principle one can design arbitrary relations between I_1 and I_2 both in phase and magnitude by tuning Z_+ and Z_-. A careful stability analysis is necessary for the experimental implementation considering that a real opamp differs from its idealized model. This shall be discussed in the following paragraphs.

D.3. Stability considerations

The skin circuit uses operational amplifiers (OpAmps) as active circuit elements to break circuit reciprocity and realize a non-Hermitian circuit Laplacian featuring skin modes. As active circuit elements can pump energy into

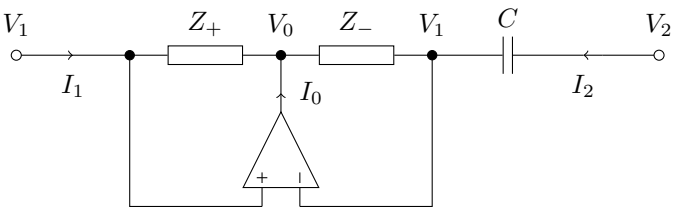

Figure S4: Circuit diagram of a negative impedance converter with current inversion (INIC). It consists of an operational amplifier (opamp) which is an active circuit element and operated in a negative feedback configuration. The opamp acts as a source or drain for currents such that unlike for all passive circuit elements $I_1 \neq -I_2$ and breaks circuit reciprocity for this reason.

the circuit, the network can become "unstable" when more energy flows into the system than dissipates. As a result, voltage accumulates at specific points. This necessarily leads to effects which are no longer described by the Laplacian formalism and the OpAmp cannot be linearized anymore. In the worst case, circuit elements in the experimental setup can be damaged. As explained below, most of these effects emerge in a *circulus vitiosus*: the accumulation of energy (in form of voltage) in the system triggers an increased energy gain and the system departs further from its linear regime. For this reason we call these effects *instabilities*.

For the present circuit setup, we classify three different types of instabilities,

(a) *local instabilities* caused by the design of the feedback loops to the operational amplifiers,

(b) *non-causal eigenmodes*, which correspond to complex eigenfrequencies causing an exponentially increasing time evolution of the eigenmode, and

(c) *saturation effects* occurring if the demanded output current of the operational amplifier exceeds its maximum output current.

Note, that the instability types (a) and (b) can occur for ideal and realistic OpAmp models, whereas type (c) occurs only for realistic OpAmps since the ideal OpAmp model is characterized by an infinitely large amplification and no limitation on output voltage or current. Moreover, the instabilities can not always be completely separated as one type can be the cause of the other types.

Instability type (a): local instabilities. Operational amplifiers are differential amplifiers. Their output voltage V_{out} is proportional to the difference of the input voltages $V_{\text{out}} = A\,(V_{\text{in},+} - V_{\text{in},-})$, where $V_{\text{in},+}$ is the positive (non-inverting) and $V_{\text{in},-}$ is the negative (inverting) input and A is the differential gain. To use an OpAmp in the INIC configuration, the output voltage is fed back to the inverting input, such that $V_{\text{in},-}$ increases (decreases) if the difference $(V_{\text{in},+} - V_{\text{in},-})$ is greater (smaller) than zero. Therefore, the output voltage fluctuates and converges to the point, where positive and negative input voltages are equal. The INIC also contains a feedback loop to the non-inverting input. The conductance in the positive feedback loop needs to be smaller than in the negative feedback loop. Otherwise, the OpAmp does not tune the input voltage difference to zero, but increases the difference further and further until the maximum output current is reached or circuit elements are damaged. In general, local instabilities in a circuit network arise as an artefact of local subnetwork structures, that are not carried on to the Laplacian, but can be inherently instable and therefore undetectable to the formalism.

Instability type (b): non-causal eigenmodes. To characterize this type of instability, we evaluate the eigenfrequencies ω_n as zeros of the eigenvalues $j_n(\omega_n) = 0$ or equivalently the poles of the Greens function G_J. For non-Hermitian systems, the eigenfrequencies are in general complex-valued. If the circuit is described by the Laplacian formalism, their imaginary part must be greater than zero. Otherwise, the circuit is unstable as one of its eigenmodes has a time-evolution $\propto e^{\alpha_n t}$ with $\alpha_n = \mathfrak{Im}\,\omega_n > 0$, which means that the circuit can never reach a steady state. Instead, the formalism predicts infinitely increasing voltages, which drive the operational amplifier out of its linear regime or damage the circuit. In terms of the circuit's Greens function, it seems like the theory violates causality (pole ω_n with $\mathfrak{Im}\,\omega_n < 0$), but is just an inconsistency in the Fourier transformation. For this reason we call the instability type (b) "non-causality".

Note, that this type of instability is always seen at all circuit nodes simultaneously, since it is caused by the collective behaviour of the circuit elements and not by local gain loops. It is triggered by an arbitrarily small excitation of the unstable eigenmode. Since the excitation of an eigenmode cannot be prevented in an experimental setup, it is important that all eigenmodes are stable. This can always be achieved by adding resistors from each node to ground. They do not change the Laplacian eigenvectors of the systems as their contribution to the Laplacian matrix is proportional to the unit matrix. The admittance eigenvalues are shifted in their real part by the inverse resistance added to the nodes and thereby add a constant global damping to the system.

Finally, note that any time-reversal symmetric but non-Hermitian system features the problem of non-causal eigenmodes and must be stabilized, because time-reversal implies, that there exists a $\omega^*(k)$ for every $\omega(k)$, which means that for a causal eigenmode with complex $\omega(\mathbf{k})$ the time-reversed partner is unstable.

Instability type (c): saturation effects. The third type of instabilities are saturation effects. Actually, these effects are not caused by poles or divergences in the system, but rather due to finite-range issues of realistic amplifiers and are not present in ideal systems. Every realistic OpAmp model exhibits an upper bound on its output power. If the driving of the system is arranged, such that the expected response exceeds the possible output of the OpAmp model, it will saturate and cut off the response at the upper limit. The saturation therefore

drives the system out of the linear regime and the response is no longer proportional to the input anymore. To lift this type of instability, one can either add more damping to the system or reduce the magnitude of the inhomogeneity. Both reduce the response of the system in different ways.

D.4. Design of the circuit board

Stabilization of non-ideal INICs. We realize a negative capacitance using the negative impedance converter (INIC) [7] introduced in Sec. D.2 of the methods. For the experimental realization of the circuit, it is crucial to take the non-idealities of the OpAmp model LT1363, which was selected in the experiment, into consideration. This includes its finite gain bandwidth product, limited stability conditions, and non-zero output impedance. Due to the complicated overall feedback loop required for our circuit, careful stability analyses was required. The OpAmp is selected to be unity-gain stable. For the concrete negative impedance configuration, an analytical analysis of the closed-loop gain generically given by

$$G_{\mathrm{CL}} = \frac{A}{1 + A\,\rho} \tag{D.12}$$

is necessary to find the required phase and gain margins for stable operation of the setup. The open-loop gain A as an intrinsic property of the OpAmp quantifies the amplification in the absence of feedback, whereas the feedback loop ρ describes the fraction of the output voltage V_0, that is fed back into the inverting input. As we choose $Z_{\mathrm{a}} = R_{\mathrm{a}}$ in the INIC setup in Sec. 1 of the methods and assume a grounded load $Z = i\omega\, C_3$, we get

$$\rho = \rho(\omega) = \frac{1}{1 + i\omega\, C_3\, R_{\mathrm{a}}} \tag{D.13}$$

as an estimate for the individual INIC configuration. It leads to instabilities if the amplification given by $A \cdot \rho$ surpasses one at the frequency, where the phase shift of $A \cdot \rho$ is equal to π, because it turns the negative feedback into an effective positive feedback. At frequencies $f > 1\,\mathrm{MHz}$, the phase shift induced by ρ is approximately $\pi/2$, which adds to the intrinsic phase shift of the OpAmp output A reaching $\pi/2$ at $f_{\mathrm{D}} \sim 1.4$ MHz. This leads to a local instability of the OpAmp at f_{D}, which can be prevented by modifying the auxiliary impedance Z_{a} by an additional parallel capacitance $C_{\mathrm{a}} = 0.47\,\mu\mathrm{F}$. This decreases the induced phase shift by ρ in such a way that the phase margin is significantly enhanced without altering the behavior of the circuit.

Eigenmode stabilization. As another type of instability, we also consider global instabilities caused by acausal eigenmodes, that correspond to eigenfrequencies with negative imaginary part. Without the incorporation of parasitic and grounding resistances, the circuit is non-Hermitian, but time-reversal symmetric. This leads to a frequency spectrum, that is symmetric upon complex conjugation, meaning every eigenfrequency has its conjugate partner. As the system is non-Hermitian and the eigenfrequencies are not constrained to the real axis, the system becomes inherently unstable. Adding a grounding resistance R_0 at all nodes shifts the frequency spectrum along the imaginary axis in the positive direction and eventually adds enough dissipation to stabilize the circuit by removing all acausal eigenfrequencies. The voltage eigenvectors remain unchanged under the insertion of R_0, but any voltage signal experiences a damping proportional to $1/R_0$ as it propagates along the chain. In the limit of strong damping, this effect leads to localized voltage profiles. A computation of the eigenfrequencies requires $R_0 \leq 45.0\,\Omega$ for PBC and $R_0 \leq 66.8\,\Omega$ for OBC to remove all global divergences.

The discrepancy of the upper bound for R_0 in the PBC and OBC system roots in the fact, that the OBC eigenvalue arcs always lie inside the PBC loops. This leads to the relation $\min(\mathfrak{Re}\,(j_{\mathrm{OBC}})) \geq \min(\mathfrak{Re}\,(j_{\mathrm{PBC}}))$ for the lowest bound OBC and PBC eigenvalue, whereas a negative real part of the admittance is prone to cause global instabilities. This is intuitively understandable, if we attach a gain and attenuation factor to every unit cell in the system. In the PBC configuration, the closed arrangement in real space forbids any unit-wise gain, as it would lead to an infinite self-reinforcement in the loop causing a divergence. In contrast, the OBC configuration as a finite system allows for simultaneous unit-wise gain and stable eigenmodes. Moreover, parasitic serial resistance may help to turn the circuit stable by increasing the upper bounds of R_0.

However, as the maximum output current of the OpAmp LT1363 is limited to $I_{\mathrm{A}} = 100\,\mathrm{mA}$, the OpAmp may still saturate even though there are no divergences in the system. Those types of instabilities can always be counteracted by exciting the skin circuit with a smaller current, as the magnitude of the voltage profile is directly proportional to the input. This property was used in the experiment in order to determine, which type of instability is present and if an adaption of R_0 is needed to lift it.

Circuit board realization. A circuit consisting of ten unit cells was implemented on a Printed Circuit Board (PCB). The measurements were done using lock-in techniques. A constant AC current was fed into one node at a time, while five lock-in amplifiers (2x Stanford Research SR 530, 2x ITHACO 3961 and AMETEK DSP7625) were used to measure the voltages at all nodes. The constant current was realized by a voltage source, that connects to the PCB through a shunt resistance of $R_S = 12.0\ \Omega$. Lock-in amplifiers were used due to their high dynamic range. This is vital for the measurement of localized bulk modes in the non-Hermitian skin effect, as the voltage drops off rapidly from the boundary and is expected to decrease in up to five orders of magnitude across ten unit cells, which needs to be resolved in an experimental voltage measurement.

While using a high dynamic range measurement equipment is essential, other practical considerations had to be taken into account. For example, strong inductive coupling between the inductors disturbed the system in such a detrimental way, that the desired behavior of the system was fundamentally obstructed. Commercially shielded inductors were not sufficiently decoupled, an extra layer of shielding by aluminum tape had to be added to them. Moreover, the circuit had to be implemented on two spatially separated circuit boards to prevent non-local couplings introducing undesired effects. The two PCBs were connected by coaxial cables. Furthermore, a metallic mesh was inserted in between the boards to minimize their coupling even further. To keep the disorder in the system to a minimum, the circuit components were pre-characterized to a tolerance of 1% by measurement of their complex impedance with an BK Precision 894 LCR meter.

Band structure measurement. The band structure measurement procedure requires measuring tens of points for a single voltage profile. In order to automate the measurements, we experimented with different multiplexing techniques. The use of mechanical relays proved impossible due to their large off-state capacitance, which caused significant coupling between nodes. CMOS based analogue multiplexers (MUX36S16 and ADG1406) were tried next, but due to their limited off-isolation and non-zero inter-channel cross-talk they caused undesired, albeit small, coupling between different nodes. Therefore, they were only used for small dynamic range measurements, where their small coupling can be neglected. Large dynamic range measurements, e.g. at selected frequencies, such as those shown in Fig. 2 of the main text, were performed manually.

References

[1] Lee, C. H. *et al.* Topolectrical circuits. *Communications Physics* **1**, 39 (2018).

[2] Helbig, T. *et al.* Band structure engineering and reconstruction in electric circuit networks. *Phys. Rev. B* **99**, 161114 (2019).

[3] Lee, T. E. Anomalous edge state in a non-hermitian lattice. *Phys. Rev. Lett.* **116**, 133903 (2016).

[4] Yao, S. & Wang, Z. Edge states and topological invariants of non-hermitian systems. *Phys. Rev. Lett.* **121**, 086803 (2018).

[5] Xiong, Y. Why does bulk boundary correspondence fail in some non-hermitian topological models. *Journal of Physics Communications* **2**, 035043 (2018).

[6] Lee, C. H. & Thomale, R. Anatomy of skin modes and topology in non-hermitian systems. *Phys. Rev. B* **99**, 201103 (2019).

[7] Hofmann, T., Helbig, T., Lee, C. H., Greiter, M. & Thomale, R. Chiral voltage propagation and calibration in a topolectrical chern circuit. *Phys. Rev. Lett.* **122**, 247702 (2019).